Temperature Compensated Dielectric Constant Sensor Using Dual-Mode Triangular Structure

Hamidreza Laribi, *Member, IEEE*, Kambiz Moez, *Senior Member, IEEE*, Hossein Rouhani, *Member, IEEE*, and Rashid Mirzavand, *Senior Member, IEEE*

***Abstract*—An aperture-coupled dual-mode triangular resonator (DMTR) sensor is presented for measuring sample under test (SUT) dielectric constant in real-time. Using this structure, it is possible to compensate for temperature variations without adding any components or circuits to the main resonator. With a specially designed slot in the middle, the proposed triangular resonator can provide two separate resonance frequencies: the lower frequency (*F*2) is used for sensing, while the upper frequency (*F*1) can be used for calibration purposes and temperature compensation. Changing the material in contact with the slot only affects *F*2, while *F*1 remains the same. A sample structure is designed and fabricated to evaluate the performance of the proposed DMTR sensor. The measurement results indicate negligible changes at *F*1 equal to 2.425 GHz, providing an acceptable calibration frequency in the industrial, scientific and medical (ISM) band. In contrast, the sample-dependent band around 2.36 GHz shifts frequency by 1.6 MHz per unit dielectric constant for samples with permittivity ranging from 1.0 to 6.15. Loss tangents of up to 0.01 are also found to have no significant effect on frequency response. Temperature analysis reveals the sensor's compensation capability. The frequency difference between *F*1 and *F*2 for any SUT remains constant over a wide temperature range from −40 °C to 140 °C. As a result, the frequency difference variations depend solely on the dielectric constant of the SUT at any given operating temperature.**

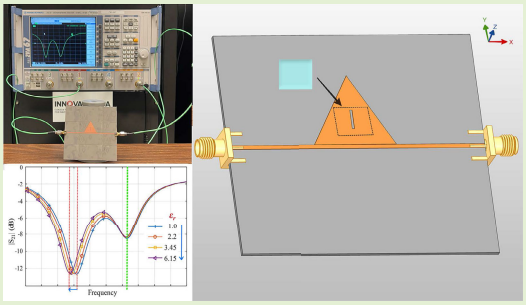

***Index Terms*— Dielectric measurement, industrial, scientific and medical (ISM) bands, sensor, temperature compensated, triangular resonator.**

I. Introduction

IN RECENT years, with the increasing development of the Internet of Things (IoT), the widespread use of sensors in industry and other environments has led to consideration of issues such as accurate performance, low cost, and long life. Using electromagnetic waves for detecting changes in a selected environment is one way to discover the variations [1]. Because of their passive structures and low cost of implementation, the planar microwave resonator sensors are widely used for different applications such as structural health monitoring [2], [3], [4], [5], environmental quality assessment [6], [7], [8], [9], human health care condition tracking [10], [11], [12], defect detection [13], [14], characterization of liquid chemicals and dielectric spectroscopy [15], [16], [17], [18], [19], [20], [21], [22], [23], [24], and mechanical displacement or rotation detection [25], [26], [27].

In planar microwave resonator sensors, those that need to be approximate to sample or material under test are of special interest because of their capability in the dielectric characterization of samples, including solid, chemical composites, liquids, and so on [28]. As a matter of fact, frequency variation is the most common working principle in microwave resonator sensors, often constructed by a planar resonator as the sensing part and loaded with a transmission line [29], [30], [31], [32].

These sensors use electromagnetic waves, mainly using fringing fields which are highly dense around the sensing region, so that changes in the sample or sample under test (SUT) cause variation in certain measurable characteristics of sensing elements such as magnitude, resonance frequency, and phase.

In recent years, researchers have examined and developed different resonance-based configurations as sensors. In [33], the coauthor proposed high-Q factor cavity structures

Manuscript received 16 May 2023; revised 27 June 2023; accepted 29 June 2023. Date of publication 18 July 2023; date of current version 15 August 2023. This work was supported in part by the National Science and Engineering Research Council of Canada (NSERC), in part by TELUS Communications Inc., in part by Future Energy Systems, and in part by CMC Microsystems. The associate editor coordinating the review of this article and approving it for publication was Dr. Wensong Wang. *(Corresponding author: Rashid Mirzavand.)*

Hamidreza Laribi, Kambiz Moez, and Rashid Mirzavand are with the Department of Electrical and Computer Engineering, University of Alberta, Edmonton, AB T6G 2R3, Canada (e-mail: hlaribi@ualberta.ca; kambiz@ualberta.ca; mirzavan@ualberta.ca).

Hossein Rouhani is with the Department of Mechanical Engineering, University of Alberta, Edmonton, AB T6G 2R3, Canada (e-mail: hrouhani@ualberta.ca).

Digital Object Identifier 10.1109/JSEN.2023.3295268

to explore the composition of liquid solutions. Microstrip transmission lines and split ring resonators (SRRs) are also widely used for sample sensing based on electromagnetic coupling [34], [35]. Moreover, researchers have investigated different incorporate of resonators to improve the accuracy of, and compensate for, different parameters such as cross-sensitivity [36], [37], [38].

In general, sensor size can play an important role in the design process. There are different planar resonator sensors useful for sensing based on frequency variations, but among them, planar semi-lumped resonators are preferred because of their small electrical size [39].

On the other hand, in reality, sensors are required an error correction rate (ECR) to estimate environmental effects such as temperature difference for precision measurements. This need in turn leads to additional building blocks, which result in higher costs and other considerations in microwave sensors. Multiple resonant frequencies are useful in different applications [40]. Although single- or dual-mode resonators have been used in filter design, dual-mode resonators are more interesting due to their benefit in the doubly tuned resonant circuits, which decrease the number of resonators by half and hence result in a compact filter configuration [41], [42]. Similarly, in resonator sensors, operation in dual modes provides the advantage of two transmission zeros which can be used for different purposes.

In general, triangular patch resonators are used for filter applications. However, each operates merely in a single mode at a specific range of frequencies [43]. Research has been conducted on triangular patch resonators as dual-mode filters [44], [45], but to the best of the authors' knowledge, neither consider it as a sensor.

Various research works have been conducted to overcome the above parameters. The authors [27], [46], [47] introduced the frequency splitting method for recognizing and compensating cross-sensitivities caused by changes in ambient factors, such as temperature. In this method, a pair of resonators are fed through a single feed line, one for sensing and the other for compensating changes in the environment. While the structure only has one feed line, it uses two resonators, which increase the sensor's dimensions. In addition, the coupling between resonators cannot be ignored, which has resulted in limited sensitivity and resolution.

Differential mode sensors are another method of considering reference frequency [48], [49], [50], [51], [52]. The introduced differential resonator sensors use two independent resonators and feed lines. Thus, the sensors are composed of two separate sensing elements and feed lines for referencing and sensing. This method eliminates the coupling limitations of the frequency split sensors but at the cost of a larger size. In addition, since the differential mode sensors are a four-port structure (two inputs, two outputs), a four-port measurement device or a two-port measurement device with some additional circuitry for transporting four ports to two ports is necessary. As a result, differential mode sensors are more expensive and complex to read than split mode sensors [53].

Contrary to [27], [46], [47], [48], [49], [50], [51], [52], and [53], the proposed dual-mode triangular resonator (DMTR) sensor uses only a single resonator with one feeding transmission line, which carries both reference and sensing frequencies simultaneously. In contrast to differential mode sensors, which use two independent resonators and feed lines (four-port structures), the proposed structure uses two distinct electromagnetic modes of a single resonator with a single feed line. Therefore, the proposed DMTR sensor effectively avoids coupling between two resonance frequencies and also cross-sensitivity of temperature. Moreover, having two sensing and reference frequencies in a single structure is effective and beneficial in different applications when variations in sensing factors do not affect reference frequency. Accordingly, the method is energy-efficient, small, low-cost, and eliminates environmental effects by combining calibration and sensing functions in a single resonator.

The proposed sensor works based on measuring the change in resonance frequencies to determine the dielectric sample properties.

The main goal of this article is to design a compact DMTR sensor with the following operation capabilities: 1) having a fixed resonance frequency as the reference point for self-calibration and/or for transferring sensor data for real-time material measurement scenarios and 2) having a sensitive resonance frequency for a wide dielectric range in a specific frequency band [industrial, scientific and medical (ISM)] to measure dielectric constant based on resonance frequency tracking. As a result of these objectives, the content is written as follows. Section II discusses the structure and operational behavior of the proposed DMTR sensor. Section III focuses on analyzing sensor performance as it approaches different sample permittivities. Section IV presents the temperature-related changes to investigate the proposed sensor in a more realistic environment. In Section V, the structure is fabricated and measured for materials with various relative permittivities. The conclusion is given in Section VI.

II. Sensor Design and Sensing Principle

A. Dual-Mode Triangular Patch Resonator

The proposed DMTR sensors use dual-mode triangular patch resonators that were originally designed as filters [44]. A triangular structure offers not only an alternative design but also a compact size and simple coupling topology when compared with dual-mode square or circular resonators. Fig. 1 presents the structure of a DMTR sensor on a dielectric substrate with a ground plane. It was discussed in [44] how the electromagnetic fields can be computed using Wheeler's cavity mode for a DMTR structure as a dual-mode resonator. The electric and magnetic fields in the z- and x-/y-directions are, respectively, equal to

$$E_z(x,y) = A_{m,n,l} \times \left\{ \cos\left[\left(\frac{2\pi x}{\sqrt{3}a} + \frac{2\pi}{3}\right)l\right] \cos\left[\frac{2\pi(m-n)y}{3a}\right] + \cos\left[\left(\frac{2\pi x}{\sqrt{3}a} + \frac{2\pi}{3}\right)m\right] \cos\left[\frac{2\pi(n-l)y}{3a}\right] + \cos\left[\left(\frac{2\pi x}{\sqrt{3}a} + \frac{2\pi}{3}\right)n\right] \cos\left[\frac{2\pi(l-m)y}{3a}\right] \right\} \tag{1a}$$

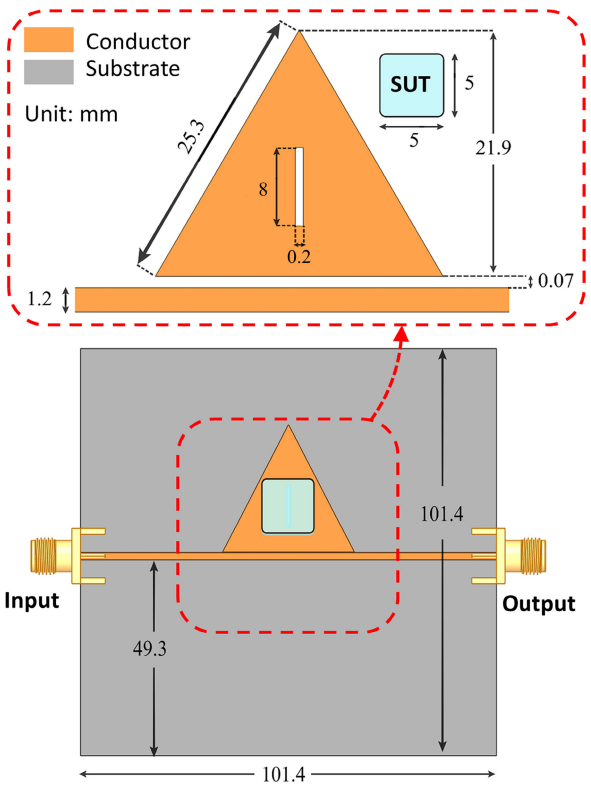

Fig. 1. Geometry of the DMTR sensor in the vicinity of the SUT.

$$H_x = \frac{j}{\omega\mu_0}\frac{\partial E_z}{\partial y} \tag{1b}$$

$$H_y = \frac{-j}{\omega\mu_0}\frac{\partial E_z}{\partial x} \tag{1c}$$

where a is the length of triangle, and $A_{m,n,l}$ is a constant coefficient. Moreover, the indexes m, n, and l should sum to zero since fields in (1) satisfy the wave equation.

By considering $\mathrm{TM}^{z}_{1,0,-1}$ as a fundamental mode (M1) for (1), and since changing the indexes m, n, and l in (1a) does not change the field pattern of the triangle, there must be another equation to find the other degeneration modes which have different field patterns, but same resonant frequency.

This problem can be solved by rotating the coordinate system and applying the principle of superposition. Accordingly, as a counterpart of (1a), the second degeneration mode can be represented by [44]

$$\begin{aligned} E_z(x,y) &= A_{1,0,-1} \\ &\times\left\{2\cos\left[\frac{\pi\left(-x+\sqrt{3}y\right)}{\sqrt{3}a}+\frac{2\pi}{3}\right]\times\cos\left[\frac{\pi\left(-\sqrt{3}x-y\right)}{3a}\right]\right. \\ &-2\cos\left[\frac{\pi\left(-x-\sqrt{3}y\right)}{\sqrt{3}a}+\frac{2\pi}{3}\right]\times\cos\left[\frac{\pi\left(\sqrt{3}x-y\right)}{3a}\right] \\ &\left.+\cos\left[\frac{2\pi\left(-\sqrt{3}x-y\right)}{3a}\right]-\cos\left[\frac{2\pi\left(\sqrt{3}x-y\right)}{3a}\right]\right\}. \end{aligned} \tag{2}$$

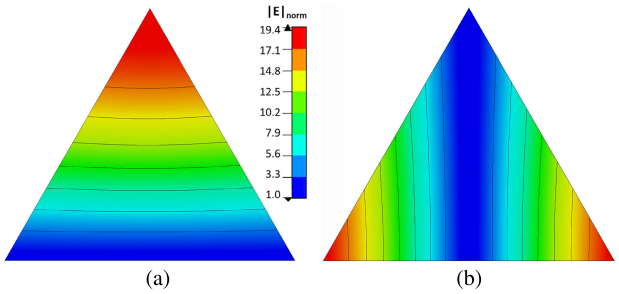

Fig. 2. Normalized electric field pattern of degeneration modes for a triangle patch resonator (a) mode 1 (M1) and (b) mode 2 (M2).

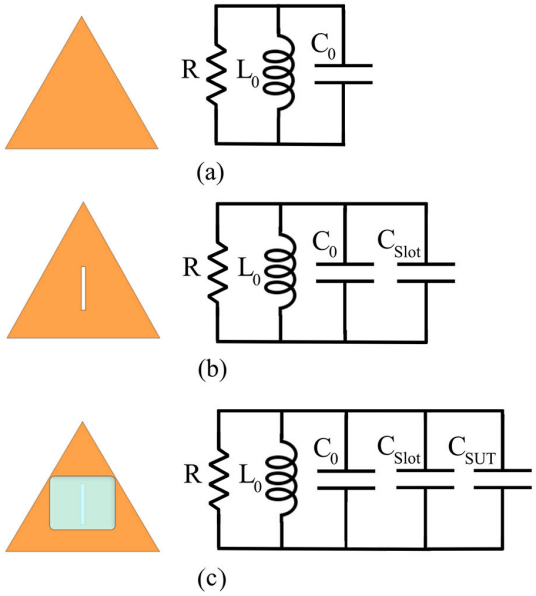

Fig. 3. Equivalent circuit model of (a) triangle resonator, (b) resonator with slot, and (c) DMTR sensor with SUT.

Using this analytical method, a pair of fundamental degenerate modes can be identified in a triangular patch resonator, with mode 1 (M1) provided by (1) and mode 2 (M2) provided by (2). These equations can be used to visualize two degeneration modes, as shown in Fig. 2.

As can be seen, M1 displays a symmetric field pattern on the vertical axis, in contrast to M2, which displays an antisymmetric field pattern.

However, the resonance frequency of M1 and M2 is equal to [37]

$$f_{m,n} = \frac{2c}{3a\sqrt{\varepsilon_r}} \tag{3}$$

where c and ε_r are speed of light and equivalent dielectric constant of substrate, respectively. The resonator and sensor analysis can be simplified by modeling the structure as an LC circuit of Fig. 3(a) with resonance frequencies of

$$F1_0 = \frac{1}{2\pi\sqrt{L_1C_1}} \tag{4}$$

$$F2_0 = \frac{1}{2\pi\sqrt{L_2C_2}} \tag{5}$$

where $L_0 \triangleq L_1 = L_2$ and $C_0 \triangleq C_1 = C_2$ are the equivalent inductance and capacitance of resonator in modes M1 and M2, respectively. In Fig. 3, R, L, and C are the resistor related

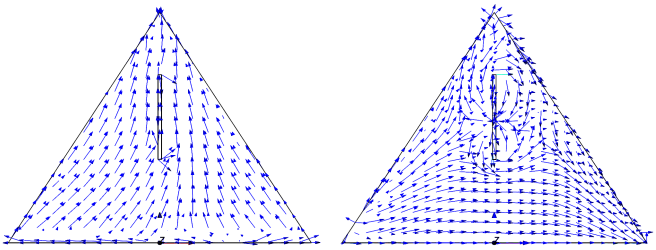

(a) (b)

Fig. 4. Current density on a triangle patch resonator of Fig. 1 (a) M1, even mode and (b) M2, odd mode.

to the equivalent loss, equivalent inductance, and equivalent capacitance of the resonator, respectively. This article uses SUTs made of nonmagnetic materials with varying dielectric constants, thereby maintaining inductance but changing capacitance, as will be shown in Section II-B.

B. DMTR Sensing and Reference Principle

In investigating the triangular resonator behavior, the aim is not only to detect relative permittivity differences among materials but also to establish a fixed-frequency reference. It will be discussed and verified in Section IV that mode splitting using a vertical slot can provide both the options at the same time.

To create a DMTR sensor, two degeneration modes (M1 and M2) of the triangular patch resonator must be split. Among various mode splitting methods [44], the best option for the DMTR sensor is a small vertical slot in the middle of the patch that can also provide a sensing point. Fig. 4 demonstrates the simulation results of surface current density, J_{surf}, for a triangular patch resonator with a vertical slot.

As can be seen, the current distribution for modes M1 and M2 is parallel and perpendicular to the vertical slot, respectively. Therefore, there is no change in the current distribution of the triangular resonator for M1 after adding a vertical slot, and C_1 remains constant. In contrast, there is a vortex of current near the slot for M2. As shown in Fig. 3(b), with the slot, a capacitance of C_{slot} is added to C_2, which shifts the resonance frequency of $F2$ downward by ΔF_{slot}, as

$$F2_{\text{slot}} = \frac{1}{2\pi\sqrt{L_2(C_2 + C_{\text{slot}})}} \triangleq F2_0 - \Delta F_{\text{slot}}. \tag{6}$$

Fig. 3(c) illustrates the equivalent circuit model of the triangular resonator considering the SUT on top of the slot. As can be seen, the SUT adds another capacitance, i.e., C_{SUT} to C_2, which reduces the resonance frequency of $F2$ more by ΔF_{SUT}, as

$$\begin{aligned} F2_{\text{SUT}} &= \frac{1}{2\pi\sqrt{L_2(C_2 + C_{\text{slot}} + C_{\text{SUT}})}} \\ &= \frac{1}{2\pi\sqrt{L_2C_2}} \cdot \frac{1}{\sqrt{1 + \frac{C_{\text{slot}}+C_{\text{SUT}}}{C_2}}} \\ &= F2_0 \\ &\quad \cdot \left(1 - \frac{C_{\text{slot}} + C_{\text{SUT}}}{2C_2} + \frac{3}{8}\frac{(C_{\text{slot}} + C_{\text{SUT}})^2}{C_2^2} + \cdots\right). \end{aligned} \tag{7}$$

TABLE I
ELECTRICAL PROPERTIES OF SUTS

Sample	Material	Dielectric constant	Loss tangent
Ref.	Air	1.00	0.0000
SUT1	RO5880	2.2	0.0009
SUT2	TMM3	3.45	0.0020
SUT3	RO3006	6.15	0.0020

In the case of $(C_{\text{slot}} + C_{\text{SUT}}) \ll C_2$, the second and higher order terms can be neglected. As SUT has no effect on $F1$, and since the resonance frequencies are initially equal, $F1 = F1_0 = F2_0$. Using $F1$ as the reference frequency and defining NDF_{SUT} as the normalized differences between two resonance frequencies for any SUT with respect to a reference SUT, i.e., Air (7) can be simplified to

$$\begin{aligned} \text{NDF}_{\text{SUT}} &\triangleq \frac{\Delta F_{\text{SUT}}}{\Delta F_{\text{Ref}}} = \frac{F1 - F2_{\text{SUT}}}{F1 - F2_{\text{Air}}} \\ &= 1 + \frac{C_{\text{SUT}}}{2C_2 - C_{\text{slot}}} \equiv 1 + \frac{\varepsilon_{\text{SUT}}}{K} \end{aligned} \tag{8}$$

or

$$\varepsilon_{\text{SUT}} = K \times \text{NDF}_{\text{SUT}} - K \tag{9}$$

where K is a constant coefficient for a specific triangle resonator with a fixed slot.

III. SIMULATION RESULTS AND DISCUSSIONS

To assess the interaction between the sensor and different materials, Ansys Electronics Desktop (HFSS) is used to design and evaluate the DMTR sensor with different sample permittivities. The sensor's behavior is investigated in a frequency range of 2.3–2.6 GHz. Fig. 1 illustrates the detailed structure of the designed sensor on a Rogers 3210 substrate with a relative permittivity of 10.8, a loss tangent of 0.0027, and a thickness of 1.27 mm. The microstrip feedline is used to excite the triangular sensor with a gap of 0.07 mm and a width of 1.2 mm, which is matched to the 50-Ω input port. In the middle of the triangular patch, there is an 8-mm-long and 0.2-mm-wide slot for illuminating and sensing the relative permittivity of an SUT. The location of SUT during all the tests is fixed, as indicated in Fig. 1. In addition, to keep errors at bay and simplify experiments, all the used SUTs have the same dimensions. The permittivity and loss tangents of these SUTs are provided in Table I.

The electric field distributions at the location of the slot inside the substrate and SUTs are plotted in Fig. 5 for both the modes and two different SUTs.

As can be seen in Fig. 5(a), at mode M1, the electric fields inside the SUTs are much less inside the substrate, hence changing the dielectric constants of SUTs has no significant effect on mode 1 of the structure. Contrary to the first mode, M1, fields strongly coupled to the SUT at the second mode M2, as shown in Fig. 5(b). Therefore, the SUT effect can be considered as an additional capacitance that will shift the resonance frequency of M2 to the lower values.

Fig. 6 displays the insertion loss and return loss results of the full-wave EM simulation for SUTs with different dielectric constant values. By observing the different variation trends of

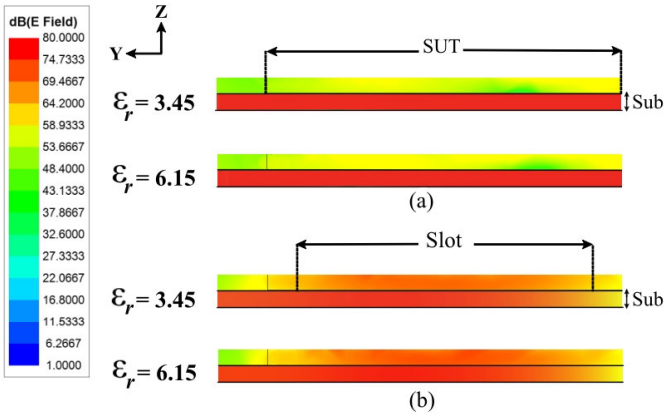

Fig. 5. Electric field distributions within the SUTs for different materials. (a) Electric field for mode 1. (b) Electric field for mode 2.

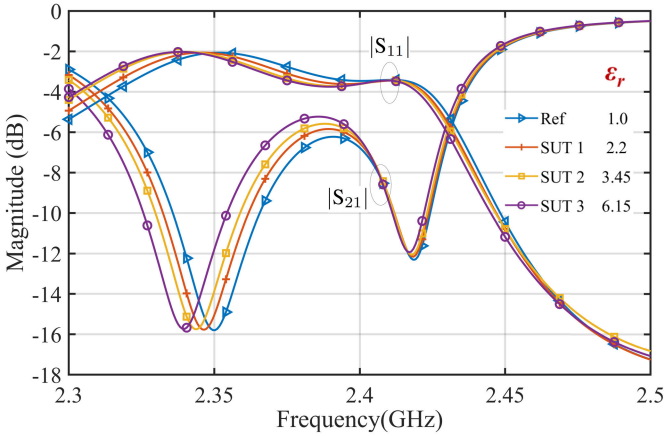

Fig. 6. Simulated insertion loss, $|S_{21}|$ (dB), and return loss $|S_{11}|$, of DMTR with reference and three SUT materials of Table I.

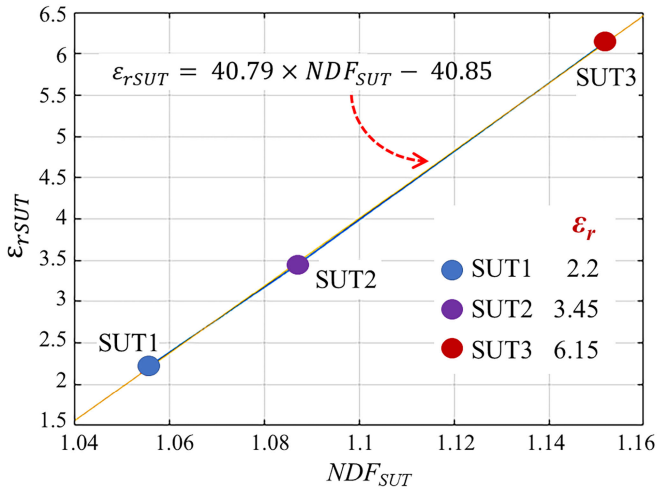

Fig. 7. Dielectric constant of SUT, ε_{rSUT}, versus normalized deviation of frequency, NDF_{SUT}, with respect to the reference, for three SUTs of Table I and the interpolated line.

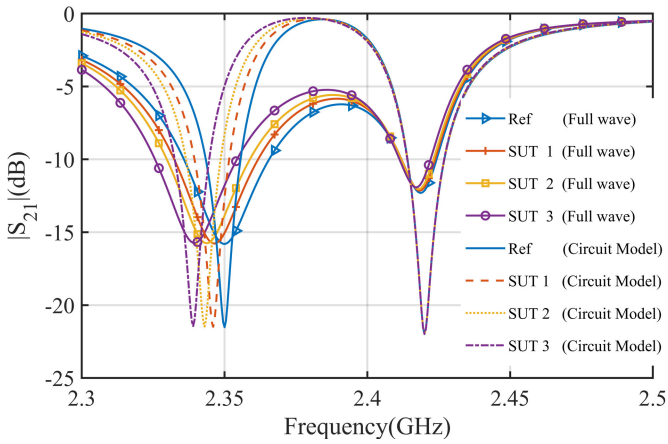

Fig. 8. Comparison between full-wave EM and circuit model simulation in the scenario with/without sample and for different SUTs of Table I.

the upper and lower frequencies, it can be approved that the lower frequency is mainly caused by the resonance in the slot, which is highly affected by sample permittivity variations.

ε_{rSUT} versus defined normalized deviation in frequency, NDF_{SUT}, is plotted in Fig. 7 for three investigated SUTs. A linear relationship between NDF_{SUT} and ε_{rSUT} can be observed in this figure as expected from (8). For the designed structure K is around 40.8.

A comparison result between full-wave simulation and circuit results obtained from ADS is presented in Fig. 8. The results show a good agreement and point out the model's validity.

A full-wave EM simulation is performed to acquire more information about the effects of dielectric loss and the thickness of the proposed structure. The results show more variation in resonance frequency by increasing the dielectric constant of SUT for the scenario with thicker SUTs. Although this sensation is less as the SUT thickness increases by a certain value.

In other words, the SUT's thickness effect on the resonant frequency variation is more notable for thinner SUTs.

This observation is because the fringing fields in the sensing region are restricted in a specific space around the narrow slot. It is a fact that sensor blindness to its surrounding area increases as it gets far from SUT.

The investigation illustrates that the physical dimensions of the SUT have a significant effect on the sensing resonance frequency of the structure. Accordingly, in practice, for different small and thin SUTs, it is preferred to have a fixed size and position relative to the DMTR sensor.

Fig. 9 demonstrates the cross-sensitivity to the thickness of SUT in the DMTR sensor. As can be seen, with increasing the SUT thickness, the variation in $F2$ frequency increases; however, the variation becomes diminished above 5 mm. Therefore, having more than 5-mm thickness in practical applications can eliminate errors due to the accuracy of SUT's thickness. Nonetheless, due to the limited availability of standard samples with a higher thickness, the same thinner SUTs were used in this study.

The samples which are shown in Table I are just to prove the fact that the variation in material relative permittivity causes a shift in the lower resonance frequency.

The SUTs can be variable permittivity materials such as pressure-depended or temperature-depended polymers as a

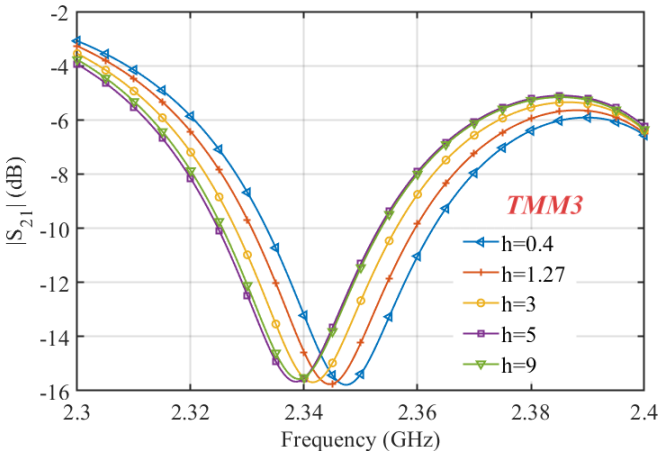

Fig. 9. Sensor cross-sensitivity to the thickness of the SUT for fixed dielectric constant TMM3.

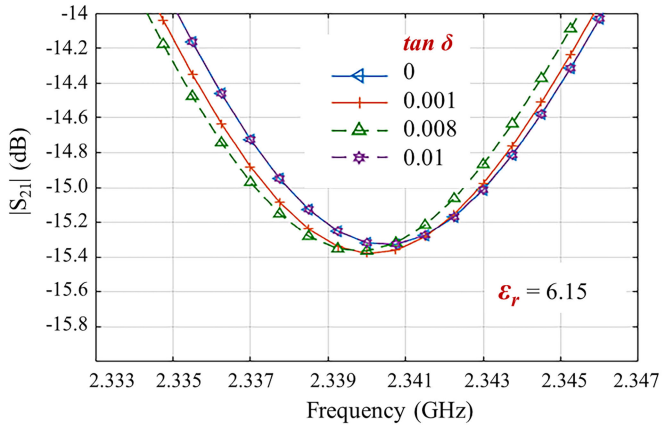

Fig. 10. Simulated insertion loss of DMTR for fictitious SUTs with a fixed dielectric constant, $\varepsilon_{rSUT} = 6.15$, and various loss tangents (tan δ from 0 to 0.01).

fixed structure that covers the narrow slot in real scenarios. In this state, the variation in the phase and resonant frequency of the DMTR sensor can be ascribed only to the changes in its dielectric constant.

Fig. 10 illustrates the effect of samples' loss in the frequency response of DMTR. In these simulations, some fictitious materials with a fixed dielectric constant, $\varepsilon_r = 6.15$, and various low loss tangents, $\tan\delta$ from 0 to 0.01, were considered as SUTs. As the reference frequency is constant, Fig. 10 only plots the response around the sensing frequency, i.e., $F2 = 2.34$ GHz. The results indicate a negligible change in the sensing resonance frequency. Thus, DMTR sensors can be used to measure dielectric constants without considering loss tangents if the SUT is not lossy.

IV. Temperature-Related Changes in Dielectric Constant

One of the main aspects of sensor design is the environment in which sensors operate, and temperature plays a main role in environmental conditions. Thus far, coating sensors is the conventional method for eliminating environmental conditions or hazards, but it increases the sensor's thickness and makes it bulkier, which is undesirable for many applications.

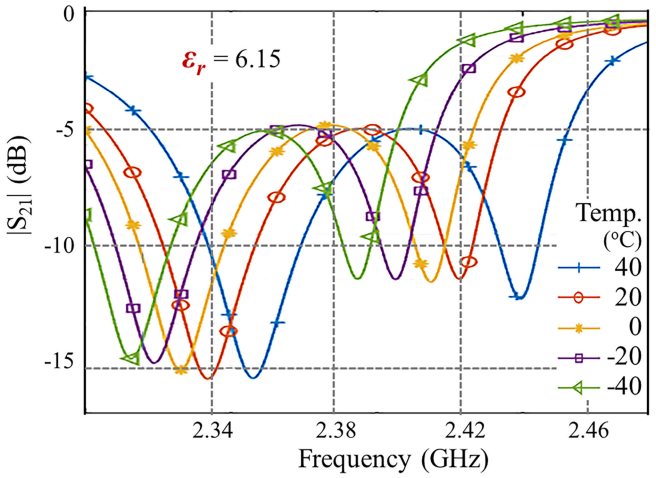

Fig. 11. Simulated insertion loss of DMTR for SUTs with a fixed dielectric constant, $\varepsilon_{rSUT} = 6.15$, and various temperatures, from -40 °C to 40 °C.

As mentioned, the sensing resonance frequency will change by changing the dielectric medium above the slot. Meanwhile, thermal expansion of conductors (ground plan and patch) and dielectric constant of dielectric material due to temperature dependency can affect the DMTR sensor.

The dielectric constant of the substrate RO3210 is 10.8 at room temperature (24 °C) and its thermal coefficient of dielectric constant (TCD_k) was found to be -459 ppm/°C for up to 150 °C. The high TCD_k leads to a high-temperature sensitivity.

Since the coefficient of thermal expansion (CTE) of the conductors is -16 ppm/°C, and the TCD_k is -459 ppm/°C, the thermal response of the DMTR sensor will be controlled by TCD_k of the substrate material. Considering the temperature effect on the dielectric layer, the variation in dielectric constant $\Delta\varepsilon_r$ can be calculated by

$$\Delta\varepsilon_r = \varepsilon_{ro} \cdot TCD_k \cdot dT \tag{10}$$

where ε_{ro} is the dielectric constant of the substrate at room temperature, and dT is the change due to temperature. To find the effect of temperature variation on DMTR response, a range is selected from -40 °C to 140 °C with steps of 20 °C. As can be seen in Fig. 11, both the resonance frequencies are shifted upward. However, the differences between two frequencies, i.e., Δf, or various temperatures remain constant for each ε_{rSUT} as illustrated in Fig. 12 for a wide temperature range from -40 °C to 140 °C. This phenomenon can be used as a self-calibration capability that will compensate the temperature dependency of resonance frequencies, and by measuring $\Delta f = (F1 - F2)$ the value of ε_{rSUT} is detectable regardless of the temperature.

V. Fabrication and Measurement

The DMTR sensor is fabricated on an RO3210 laminate substrate. Two coaxial connectors are soldered to the feedline's input and output to analyze the sensor. The R&SZVA13 vector network analyzer (VNA) is connected to the input and output ports to measure the S-parameters, as shown in Fig. 13.

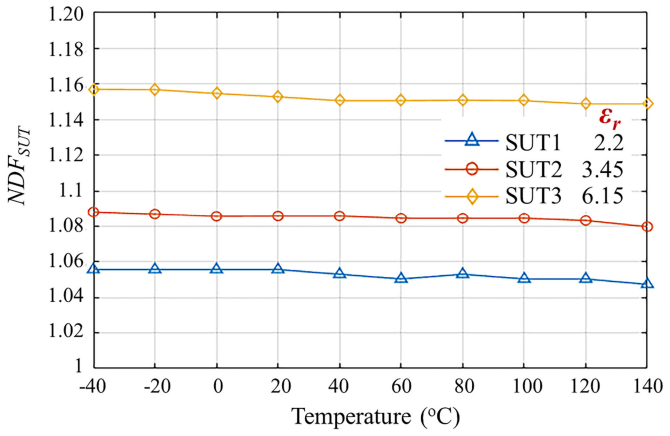

Fig. 12. Simulated normalized deviation in resonance frequency, NDF_{SUT}, of DMTR in a wide temperature range from −40 °C to 140 °C for three SUTs.

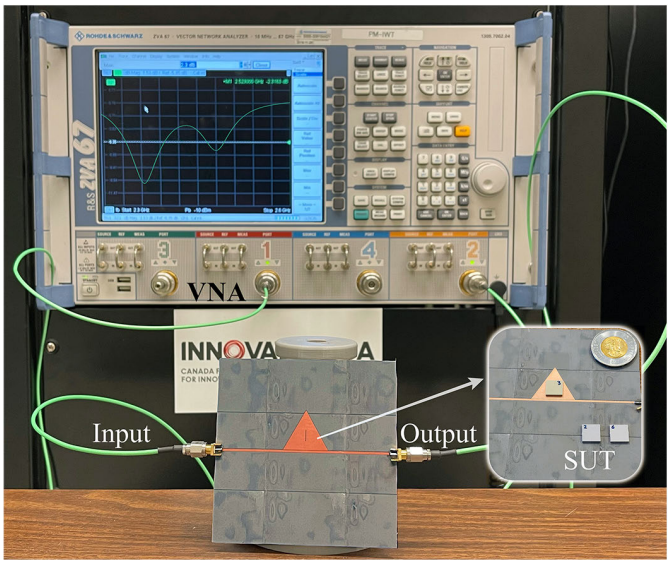

Fig. 13. Measurement setup using a VNA and equal-sized SUTs. The samples were taken from standard dielectric substrates.

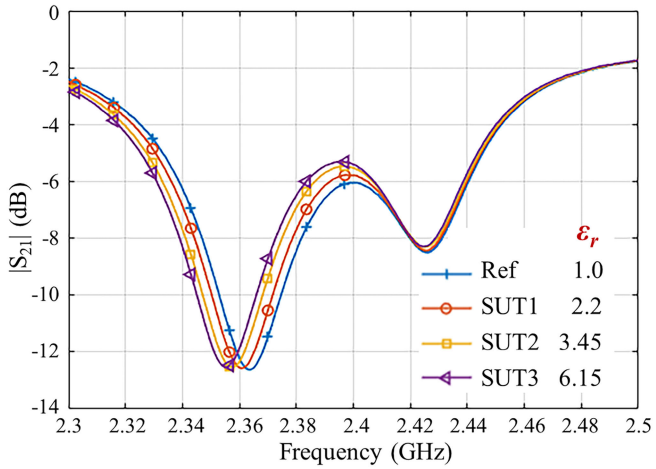

Fig. 14. Measured insertion loss, $|S_{21}|$ (dB), of DMTR with reference and three SUT materials of Table I.

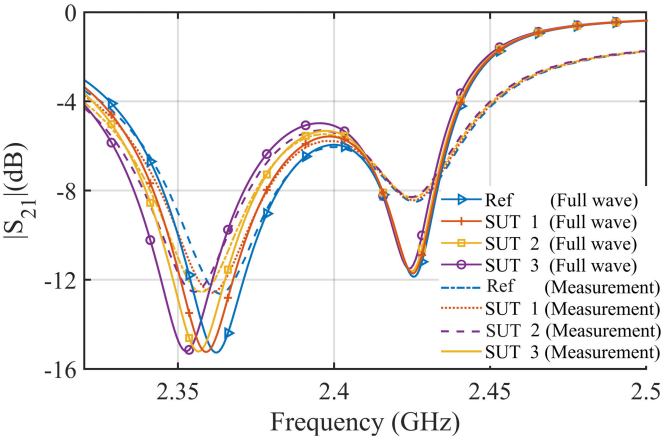

Fig. 15. Comparison between full-wave EM simulation and measurement in the scenario with/without sample and for different SUTs of Table I.

Small rectangular cubes of materials with dimensions of $5 \times 5 \times 1.27$ mm are placed in the center of the structure as SUTs. Then for each setup, SUTs with the same dimensions are tightly fixed over the narrow slot to reduce the unwanted air gap between the sample and the DMTR sensor.

Fig. 14 demonstrates the measurement results for different SUTs with relative permittivities between 1 and 6.15. As shown in this figure, the reference frequency $F1$ is about 2.425 GHz. As expected, the frequency of $F1$ does not change while the sensor frequency $F2$ varies between 2.365 and 2.355 GHz. Therefore, samples whose permittivity ranges from 1 to 6.15 can be detected using the fabricated sensor with a frequency shift of 1.6 MHz per unit dielectric constant. Due to fabrication inaccuracies, the simulation and measurement frequencies differ slightly. Since the substrate RO3210 has a tolerance of $+/-0.5$, the EM simulation results were refined and the relative permittivity of 10.7 was considered in the fabricated sensor for further comparison. Moreover, a gap of 0.04 mm was added to the design to increase accuracy between full-wave simulation and real scenarios.

After modification, a comparison between EM full-wave simulation and measurement results is demonstrated in Fig. 15. As can be seen, there is a good following between the simulation and measurement. In accordance with expectations, the higher resonance frequency is situated constantly during changing materials; in contrast, the lower frequency is sensitive to the relative permittivity of materials and decreased by increasing the dielectric constant in the sensing region.

Fig. 16 illustrates the measurement and EM full-wave simulation results of three different temperatures for an SUT with a relative permittivity of 3.15. The measurement setup is conducted in controlled surroundings. The experimental setup consists of a VNA, sealed box, thermometer, heat source, and power supply.

As discussed in Section IV, the thermal expansion of dielectric constant of dielectric material and conductors due to temperature dependency can affect the DMTR sensor. Although due to the high sensitivity of substrate TCD_k (−459 ppm/°C), the thermal response of the DMTR sensor

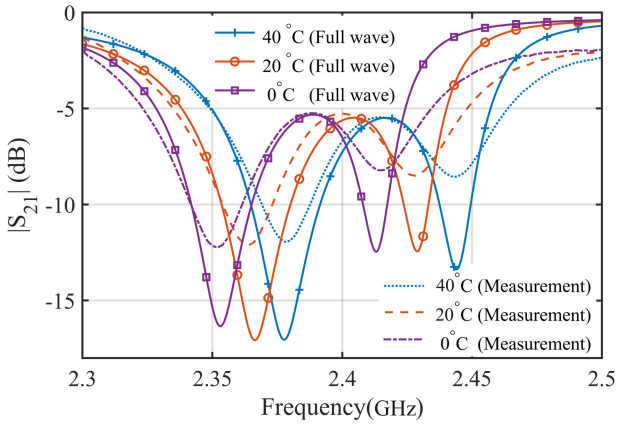

Fig. 16. Insertion loss related to full-wave EM simulation and measurement results of the proposed DMTR sensor for three different temperatures.

will be controlled by TCD_k of the substrate material, and the variation in dielectric constant can be calculated by (10). As can be seen in Fig. 16, increasing the temperature pushes both the resonance frequencies upward; however, the difference between the two frequencies remains constant for each ε_{rSUT}. In this way, the temperature dependency of resonance frequencies can be compensated. Moreover, according to the comparison results for the mentioned temperature range and NDF_{SUT} (Fig. 12), for various SUTs, the accuracy is constant for the mentioned temperature range with a 0.86% error.

Different SUTs exhibit a comparatively significant shift in the sensing resonance frequency. All the samples examined have low dielectric loss values, and based on Fig. 10, the frequency shifts in $F2$ are caused by the changes in the real part of the sample's dielectric constant, i.e., ε_{rSUT}.

In microwave frequency-based sensors, as the main figure of merit, the comparison is often based on the relative sensitivity of the resonance frequency, which is defined as

$$S_{av,f} = \frac{1}{f_0}\frac{df_0}{d\varepsilon_r}. \tag{11}$$

A meaningful comparison between microwave permittivity sensors based on frequency variation reported in the literature is difficult due to the fact that in other designs there is no restriction on total frequency shift for a wide range of SUTs to maintain response in the standard ISM band. Therefore, for the sake of fairness, the proposed design is considered in its maximum sensitivity which releases the limited parameters. So that the SUTs' thickness increased to 5 mm, and the gap between the feed line and the triangle decreased by a value of 0.04 mm.

Table II shows a comparison between the proposed dual-mode DMTR sensor and the state-of-the-art designs. It summarizes some characteristics of various sensors for measuring dielectric constants, including their operation frequency, working principle, and accuracy which is shown by sensitivity. Here, f_0 is the resonance frequency of the sensor without SUT (bare sensor), and S_{av} is the sensor sensitivity defined in (11). Since different sensors operate in different frequencies, and for having fair comparison $\overline{S}_{av}$ is the one that should be considered in comparison such that $\overline{S}_{av}$, derived by dividing S_{av} by the central frequency, f_0, of the frequency span.

TABLE II
COMPARISON OF VARIOUS SENSORS IN TERMS OF SENSITIVITY

Reference	f_0(GHz)	S_{av}(MHz)	$\overline{S}_{av}$(%)	Working Principle
[30]	2	6.8	0.34	Frequency variation
[21]	2.365	0.9	0.038	Frequency variation
[46]	0.978	2.03	0.207	Frequency splitting
[48]	1.125	4.24	0.376	Differential
[22]	2.4	4.9	0.2	Frequency variation
This work*	**2.4**	**13.98**	**0.58**	**Frequency splitting**

*This is the obtained results in the maximum situation.

VI. CONCLUSION

A high-resolution doubly loaded triangular sensor is used to measure different dielectric substrates. The higher resonance frequency of this sensor is used for self-calibration purposes because of its stability and intended frequency range. The sensing resonance frequency ($F2$) has shown a comparatively considerable shift for material with different relative permittivities. The effect of temperature on sensor performance is compensated by considering the difference between two resonance frequencies, which is constant with respect to the temperature.

REFERENCES

[1] E. Nyfors, "Industrial microwave sensors—A review," *Subsurface Sens. Technol. Appl.*, vol. 1, pp. 23–43, Jan. 2000.
[2] Z. Liu and Y. Kleiner, "State-of-the-art review of technologies for pipe structural health monitoring," *IEEE Sensors J.*, vol. 12, no. 6, pp. 1987–1992, Jun. 2012.
[3] B. S. Cook, A. Shamim, and M. M. Tentzeris, "Passive low-cost inkjet-printed smart skin sensor for structural health monitoring," *IET Microw., Antennas Propag.*, vol. 6, no. 14, pp. 1536–1541, Nov. 2012.
[4] A. M. J. Marindra and G. Y. Tian, "Chipless RFID sensor tag for metal crack detection and characterization," *IEEE Trans. Microw. Theory Techn.*, vol. 66, no. 5, pp. 2452–2462, May 2018.
[5] W. Wang et al., "Wideband gain enhancement of MIMO antenna and its application in FMCW radar sensor integrated with CMOS-based transceiver chip for human respiratory monitoring," *IEEE Trans. Antennas Propag.*, vol. 71, no. 1, pp. 318–329, Jan. 2023.
[6] R. Mirzavand, M. Honari, B. Laribi, B. Khorshidi, M. Sadrzadeh, and P. Mousavi, "An unpowered sensor node for real-time water quality assessment (Humic Acid Detection)," *Electronics*, vol. 7, no. 10, p. 231, Oct. 2018.
[7] M. Islam, F. Ashraf, T. Alam, N. Misran, and K. Mat, "A compact ultrawideband antenna based on hexagonal split-ring resonator for pH sensor application," *Sensors*, vol. 18, no. 9, p. 2959, Sep. 2018.
[8] R. Mirzavand and P. Mousavi, "A ZERO-power sensor using multi-port direct-conversion sensing," *IEEE Sensors J.*, vol. 18, no. 22, pp. 9243–9250, Nov. 2018.
[9] H. Saghlatoon, R. Mirzavand, M. M. Honari, and P. Mousavi, "Sensor antenna transmitter system for material detection in wireless-sensor-node applications," *IEEE Sensors J.*, vol. 18, no. 21, pp. 8812–8819, Nov. 2018.
[10] K. Grenier et al., "Integrated broadband microwave and microfluidic sensor dedicated to bioengineering," *IEEE Trans. Microw. Theory Techn.*, vol. 57, no. 12, pp. 3246–3253, Dec. 2009.
[11] A. Tamra, D. Dubuc, M.-P. Rols, and K. Grenier, "Microwave monitoring of single cell monocytes subjected to electroporation," *IEEE Trans. Microw. Theory Techn.*, vol. 65, no. 9, pp. 3512–3518, Sep. 2017.

[12] J. Kilpijärvi, J. Tolvanen, J. Juuti, N. Halonen, and J. Hannu, "A non-invasive method for hydration status measurement with a microwave sensor using skin phantoms," *IEEE Sensors J.*, vol. 20, no. 2, pp. 1095–1104, Jan. 2020.

[13] W. Wang et al., "Analysis and design of coil-based electromagnetic-induced thermoacoustic for rail internal-flaw inspection," *IEEE Trans. Intell. Transp. Syst.*, vol. 20, no. 7, pp. 2691–2702, Jul. 2019.

[14] W. Wang et al., "Novel coil transducer induced thermoacoustic detection of rail internal defects towards intelligent processing," *IEEE Trans. Ind. Electron.*, early access, Mar. 6, 2023, doi: 10.1109/TIE.2023.3250766.

[15] M. H. Zarifi, S. Farsinezhad, K. Shankar, and M. Daneshmand, "Liquid sensing using active feedback assisted planar microwave resonator," *IEEE Microw. Wireless Compon. Lett.*, vol. 25, no. 9, pp. 621–623, Sep. 2015.

[16] H. Saghlatoon, R. Mirzavand, and P. Mousavi, "Fixed-frequency low-loss dielectric material sensing transmitter," *IEEE Trans. Ind. Electron.*, vol. 68, no. 4, pp. 3517–3526, Apr. 2021.

[17] C.-S. Lee and C.-L. Yang, "Thickness and permittivity measurement in multi-layered dielectric structures using complementary split-ring resonators," *IEEE Sensors J.*, vol. 14, no. 3, pp. 695–700, Mar. 2014.

[18] R. A. Alahnomi, Z. Zakaria, E. Ruslan, S. R. A. Rashid, and A. A. M. Bahar, "High-Q sensor based on symmetrical split ring resonator with spurlines for solids material detection," *IEEE Sensors J.*, vol. 17, no. 9, pp. 2766–2775, May 2017.

[19] R. Mirzavand, M. M. Honari, and P. Mousavi, "Direct-conversion sensor for wireless sensing networks," *IEEE Trans. Ind. Electron.*, vol. 64, no. 12, pp. 9675–9682, Dec. 2017.

[20] J. Muñoz-Enano, P. Vélez, M. Gil, and F. Martín, "Frequency-variation sensors for permittivity measurements based on dumbbell-shaped defect ground structures (DB-DGS): Analytical method and sensitivity analysis," *IEEE Sensors J.*, vol. 22, no. 10, pp. 9378–9386, May 2022.

[21] E. L. Chuma, Y. Iano, G. Fontgalland, and L. L. B. Roger, "Microwave sensor for liquid dielectric characterization based on metamaterial complementary split ring resonator," *IEEE Sensors J.*, vol. 18, no. 24, pp. 9978–9983, Dec. 2018.

[22] X. Zhang, C. Ruan, T. Haq, and K. Chen, "High-sensitivity microwave sensor for liquid characterization using a complementary circular spiral resonator," *Sensors*, vol. 19, no. 4, p. 787, Feb. 2019.

[23] E. L. Chuma and T. Rasmussen, "Metamaterial-based sensor integrating microwave dielectric and near-infrared spectroscopy techniques for substance evaluation," *IEEE Sensors J.*, vol. 22, no. 20, pp. 19308–19314, Oct. 2022.

[24] E. L. Chuma and Y. Iano, "Novelty sensor using integrated fluorescence and dielectric spectroscopy to improve food quality identification," in *Proc. IEEE Sensors*, Oct. 2022, pp. 1–4.

[25] J. Naqui, M. Durán-Sindreu, and F. Martín, "Alignment and position sensors based on split ring resonators," *Sensors*, vol. 12, no. 9, pp. 11790–11797, Aug. 2012.

[26] A. Ebrahimi, W. Withayachumnankul, S. F. Al-Sarawi, and D. Abbott, "Metamaterial-inspired rotation sensor with wide dynamic range," *IEEE Sensors J.*, vol. 14, no. 8, pp. 2609–2614, Aug. 2014.

[27] A. K. Horestani, J. Naqui, D. Abbott, C. Fumeaux, and F. Martín, "Two-dimensional displacement and alignment sensor based on reflection coefficients of open microstrip lines loaded with split ring resonators," *Electron. Lett.*, vol. 50, no. 8, pp. 620–622, Apr. 2014.

[28] J. Muñoz-Enano, P. Vélez, M. Gil, and F. Martín, "Planar microwave resonant sensors: A review and recent developments," *Appl. Sci.*, vol. 10, no. 7, p. 2615, Apr. 2020.

[29] W. Withayachumnankul, K. Jaruwongrungsee, A. Tuantranont, C. Fumeaux, and D. Abbott, "Metamaterial-based microfluidic sensor for dielectric characterization," *Sens. Actuators A, Phys.*, vol. 189, pp. 233–237, Jan. 2013.

[30] A. Ebrahimi, W. Withayachumnankul, S. Al-Sarawi, and D. Abbott, "High-sensitivity metamaterial-inspired sensor for microfluidic dielectric characterization," *IEEE Sensors J.*, vol. 14, no. 5, pp. 1345–1351, May 2014.

[31] A. Salim and S. Lim, "Complementary split-ring resonator-loaded microfluidic ethanol chemical sensor," *Sensors*, vol. 16, no. 11, p. 1802, Oct. 2016.

[32] C.-L. Yang, C.-S. Lee, K.-W. Chen, and K.-Z. Chen, "Noncontact measurement of complex permittivity and thickness by using planar resonators," *IEEE Trans. Microw. Theory Techn.*, vol. 64, no. 1, pp. 247–257, Jan. 2016.

[33] G. Gennarelli, S. Romeo, M. R. Scarfì, and F. Soldovieri, "A microwave resonant sensor for concentration measurements of liquid solutions," *IEEE Sensors J.*, vol. 13, no. 5, pp. 1857–1864, May 2013.

[34] R. Mirzavand, M. M. Honari, and P. Mousavi, "High-resolution balanced microwave material sensor with extended dielectric range," *IEEE Trans. Ind. Electron.*, vol. 64, no. 2, pp. 1552–1560, Feb. 2017.

[35] R. Mirzavand, M. M. Honari, and P. Mousavi, "High-resolution dielectric sensor based on injection-locked oscillators," *IEEE Sensors J.*, vol. 18, no. 1, pp. 141–148, Jan. 2018.

[36] S. Xue, Z. Yi, L. Xie, G. Wan, and T. Ding, "A passive wireless crack sensor based on patch antenna with overlapping sub-patch," *Sensors*, vol. 19, no. 19, p. 4327, Oct. 2019.

[37] Y. Seo, M. U. Memon, and S. Lim, "Microfluidic eighth-mode substrate-integrated-waveguide antenna for compact ethanol chemical sensor application," *IEEE Trans. Antennas Propag.*, vol. 64, no. 7, pp. 3218–3222, Jul. 2016.

[38] S. Xue, Z. Yi, L. Xie, G. Wan, and T. Ding, "A displacement sensor based on a normal mode helical antenna," *Sensors*, vol. 19, no. 17, p. 3767, Aug. 2019.

[39] M. Durán-Sindreu, J. Naqui, F. Paredes, J. Bonache, and F. Martín, "Electrically small resonators for planar metamaterial, microwave circuit and antenna design: A comparative analysis," *Appl. Sci.*, vol. 2, no. 2, pp. 375–395, Apr. 2012.

[40] W. Wang and Y. Zheng, "Wideband gain enhancement of high-isolation Fabry–Pérot antenna array with tandem circular parasitic patches and radial gradient PRS," *IEEE Trans. Antennas Propag.*, vol. 69, no. 11, pp. 7959–7964, Nov. 2021.

[41] L. Athukorala and D. Budimir, "Compact dual-mode open loop microstrip resonators and filters," *IEEE Microw. Wireless Compon. Lett.*, vol. 19, no. 11, pp. 698–700, Nov. 2009.

[42] J.-S. Hong, H. Shaman, and Y.-H. Chun, "Dual-mode microstrip open-loop resonators and filters," *IEEE Trans. Microw. Theory Techn.*, vol. 55, no. 8, pp. 1764–1770, Aug. 2007.

[43] J.-S. Hong and M. J. Lancaster, "Microstrip triangular patch resonator filters," in *IEEE MTT-S Int. Microw. Symp. Dig.*, Jun. 2000, pp. 331–334.

[44] J.-S. Hong and S. Li, "Theory and experiment of dual-mode microstrip triangular patch resonators and filters," *IEEE Trans. Microw. Theory Techn.*, vol. 52, no. 4, pp. 1237–1243, Apr. 2004.

[45] J.-S. Hong and S. Li, "Dual-mode microstrip triangular patch resonators and filters," in *IEEE MTT-S Int. Microw. Symp. Dig.*, Jun. 2003, pp. 1901–1904.

[46] P. Vélez, L. Su, K. Grenier, J. Mata-Contreras, D. Dubuc, and F. Martín, "Microwave microfluidic sensor based on a microstrip splitter/combiner configuration and split ring resonators (SRRs) for dielectric characterization of liquids," *IEEE Sensors J.*, vol. 17, no. 20, pp. 6589–6598, Oct. 2017.

[47] L. Su, J. Mata-Contreras, P. Vélez, and F. Martín, "Splitter/combiner microstrip sections loaded with pairs of complementary split ring resonators (CSRRs): Modeling and optimization for differential sensing applications," *IEEE Trans. Microw. Theory Techn.*, vol. 64, no. 12, pp. 4362–4370, Dec. 2016.

[48] P. Vélez, K. Grenier, J. Mata-Contreras, D. Dubuc, and F. Martín, "Highly-sensitive microwave sensors based on open complementary split ring resonators (OCSRRs) for dielectric characterization and solute concentration measurement in liquids," *IEEE Access*, vol. 6, pp. 48324–48338, 2018.

[49] P. Vélez, J. Muñoz-Enano, K. Grenier, J. Mata-Contreras, D. Dubuc, and F. Martín, "Split ring resonator-based microwave fluidic sensors for electrolyte concentration measurements," *IEEE Sensors J.*, vol. 19, no. 7, pp. 2562–2569, Apr. 2019.

[50] J. Muñoz-Enano et al., "Microstrip lines loaded with metamaterial-inspired resonators for microwave sensors/comparators with optimized sensitivity," in *Proc. 49th Eur. Microw. Conf. (EuMC)*, Oct. 2019, pp. 754–757.

[51] P. Vélez, J. Muñoz-Enano, and F. Martín, "Electrolyte concentration measurements in DI water with 0.125 g/L resolution by means of CSRR-based structures," in *Proc. 49th Eur. Microw. Conf. (EuMC)*, Oct. 2019, pp. 340–343.

[52] A. Ebrahimi, J. Scott, and K. Ghorbani, "Differential sensors using microstrip lines loaded with two split-ring resonators," *IEEE Sensors J.*, vol. 18, no. 14, pp. 5786–5793, Jul. 2018.

[53] J. Muñoz-Enano, P. Velez, M. Gil, and F. Martín, "Microfluidic reflective-mode differential sensor based on open split ring resonators (OSRRs)," *Int. J. Microw. Wireless Technol.*, vol. 12, pp. 1–10, May 2020.

Hamidreza Laribi (Member, IEEE) received the master's degree in telecommunication engineering, majoring in RF systems design and electromagnetic compatibility, from the Amirkabir University of Technology, Tehran, Iran, in 2016. He is currently pursuing the Ph.D. degree in electrical engineering with the Department of Electrical Engineering, University of Alberta, Edmonton, AB, Canada.

He joined the Intelligent Wireless Technologies Laboratory (IWT), University of Alberta, as a Research Assistant in 2020. His current research interests include designing radio frequency identification (RFID) wireless sensing architectures and sensors for a wide range of physical parameters' measurement.

Kambiz Moez (Senior Member, IEEE) received the B.Sc. degree in electrical engineering from the University of Tehran, Tehran, Iran, in 1999, and the M.Sc. and Ph.D. degrees from the University of Waterloo, Waterloo, ON, Canada, in 2002 and 2006, respectively.

Since January 2007, he has been with the Department of Electrical and Computer Engineering, University of Alberta, Edmonton, AB, Canada, where he is currently a Professor. His research interests include analysis and design of analog, radio frequency, and millimeter-wave CMOS integrated circuits and systems for a variety of applications, including wired/wireless communications, biomedical imaging, instrumentations, radars, and power electronics.

Dr. Moez is serving as an Associate Editor for the IEEE TRANSACTIONS ON CIRCUITS AND SYSTEMS I: REGULAR PAPERS and *IET Electronic Letters*. He is also a Registered Professional Engineer in the Province of Alberta.

Hossein Rouhani (Member, IEEE) received the B.Sc. degree in mechanical engineering from the Amirkabir University of Technology, Tehran, Iran, in 2002, the M.Sc. degree in mechanical engineering from the University of Tehran, Tehran, in 2005, and the Ph.D. degree in biotechnology and bioengineering from the Swiss Federal Institute of Technology in Lausanne (EPFL), Lausanne, Switzerland, in 2010.

He was a Postdoctoral Fellow at the University of Toronto, Toronto, ON, Canada, from 2012 to 2015. He is currently an Associate Professor with the Department of Mechanical Engineering, University of Alberta, Edmonton, AB, Canada. His research interests include biomedical instrumentation design and development of rehabilitative technologies.

Dr. Rouhani is an Associate Editor for the IEEE CANADIAN JOURNAL OF ELECTRICAL AND COMPUTER ENGINEERING, *Transactions of the Canadian Society for Mechanical Engineering*, and *Frontiers in Sports and Active Living*.

Rashid Mirzavand (Senior Member, IEEE) received the B.Sc. degree from the Isfahan University of Technology, Isfahan, Iran, in 2004, and the M.Sc. and Ph.D. degrees from the Amirkabir University of Technology (Tehran Polytechnic), Tehran, Iran, in 2007 and 2011, respectively, all in electrical engineering.

He is currently an Assistant Professor with the Department of Electrical and Computer Engineering, University of Alberta, Edmonton, AB, Canada, where he leads the Intelligent Wireless Technology Group. He is also an Adjunct Fellow with the Faculty of Engineering and Information Technology (IT), University of Technology Sydney, Sydney, NSW, Australia. He has three granted and eight filed U.S. patents and is a (co)author of more than 100 journals and 70 conference papers. His major research interests include, but are not limited to, RF/microwave/mm-wave circuits, sensors, reconfigurable intelligent surfaces and antennas, numerical methods, and measurement systems.

Dr. Mirzavand received various awards, such as the Best Amirkabir University of Technology (AUT) M.Sc. Researcher in 2007, the Best AUT Ph.D. Researcher in 2011, the Best Ministry of Information and Communications Technology (MICT) National Researcher in 2013, the National Elite Foundation Young Professor Grant in 2014, the Alberta Innovates – Technology Futures (AITF) Elite Postdoctoral Fellowship (PDF) in 2015, the Honorable Canadian Microelectronics Corporation (CMC) Industrial Collaboration in 2017, the TEC Edmonton Innovation in 2019, the CMC Industrial Collaboration in 2021 as the Supervisor, the University of Alberta (UofA) Innovation in 2021, and three UofA Innovation in 2022. He is a Registered Member of the Association of Professional Engineers and Geoscientists of Alberta. He serves as the Specialty Chief Editor for *Frontiers in the Internet of Things* (IoT Enabling Technologies Section).